J Nonlinear Sci (2015) 25:709–739
DOI 10.1007/s00332-015-9239-8

Journal of Nonlinear Science

On the Gross–Pitaevskii Equation with Pumping and Decay: Stationary States and Their Stability

Jesús Sierra · Aslan Kasimov · Peter Markowich · Rada-Maria Weishäupl

Received: 11 November 2013 / Accepted: 26 January 2015 / Published online: 11 February 2015
© Springer Science+Business Media New York 2015

Abstract We investigate the behavior of solutions of the complex Gross–Pitaevskii equation, a model that describes the dynamics of pumped decaying Bose–Einstein condensates. The stationary radially symmetric solutions of the equation are studied, and their linear stability with respect to two-dimensional perturbations is analyzed. Using numerical continuation, we calculate not only the ground state of the system, but also a number of excited states. Accurate numerical integration is employed to study the general nonlinear evolution of the system from the unstable stationary solutions to the formation of stable vortex patterns.

Keywords Complex Gross–Pitaevskii equation · Numerical continuation · Collocation method · Bose–Einstein condensate

Communicated by Edriss S. Titi.

Electronic supplementary material The online version of this article (doi:10.1007/s00332-015-9239-8) contains supplementary material, which is available to authorized users.

J. Sierra · A. Kasimov (✉) · P. Markowich
King Abdullah University of Science and Technology, Box 4700, Thuwal 23955-6900, Saudi Arabia
e-mail: aslan.kasimov@kaust.edu.sa

J. Sierra
e-mail: jesus.sierra@kaust.edu.sa

P. Markowich
e-mail: peter.markowich@kaust.edu.sa

R.-M. Weishäupl
Faculty of Mathematics, Vienna University, Oskar-Morgenstern-Platz 1, 1090 Wien, Austria
e-mail: rada.weishaeupl@univie.ac.at

1 Introduction

In this paper, we explore numerically the behavior of solutions of the complex Gross–Pitaevskii (GP) equation:

$$i\psi_t = -\Delta\psi + V(x)\psi + |\psi|^2\psi + i\left[\omega(x) - \sigma|\psi|^2\right]\psi, t > 0, \quad x \in D = \mathbb{R}^2,$$
$$\psi(x,0) = \psi_0(x), \quad x \in D, \tag{1}$$

where $\psi = \psi(x,t)$ represents the wave function, $V(x)$ is the trapping potential, $\omega = \omega(x) \geq 0$ is the pumping term, and $\sigma > 0$ is the strength of the decaying term. Equation (1) was proposed by Keeling and Berloff (2008) to study pumped decaying condensates, particularly the Bose–Einstein condensates (BEC) of exciton–polaritons.

We use accurate numerical techniques to investigate the nature of the radially symmetric stationary solutions of (1), their linear stability properties, and the long-time nonlinear evolution of the solutions of (1) that start with the unstable stationary states as initial conditions. The stationary radially symmetric solutions of the complex GP equation are computed by using a numerical collocation method. Such stationary solutions are found to be linearly unstable with respect to two-dimensional perturbations when the pumping region is small as well as when it is large. Linearly stable solutions are used as a starting point in a numerical continuation method, wherein the stationary solutions are computed when a parameter in the equation is varied. A number of different stationary solutions are found at any given set of parameters. Among these solutions, the linearly stable one is seen to have the smallest chemical potential. Such solution is denoted as the ground state, while the other solutions are termed the excited states. With the stationary solutions and their linear stability properties known, we then implement a time-splitting spectral method to solve (1) and explore the nonlinear dynamics of the solutions.

The GP equation and its variants are widely used to understand BEC in various systems. The possibility of condensation of bosons was predicted by Bose (1924) and Einstein (1924, 1925). The condensate was obtained experimentally for the first time in Anderson et al. (1995), Bradley et al. (1995), and Davis et al. (1995) in a system consisting of about half a million alkali atoms cooled down to nanokelvin-level temperatures. The principal interest in BEC lies in its nature as a macroscopic quantum system. Some of the dynamics of atomic BEC have been successfully described by the GP equation (Gross 1963; Pitaevskii 1961; Pitaevskii and Stringari 2003), a nonlinear Schrödinger equation,

$$i\hbar\psi_t = -\frac{\hbar^2}{2m}\Delta\psi + V(\mathbf{x})\psi + \delta|\psi|^2\psi, \tag{2}$$

derived from the mean field theory of weakly interacting bosons. Here, $\psi = \psi(\mathbf{x},t)$ is the wave function of the condensate, δ is a constant characterizing the strength of the boson-boson interactions, m is the mass of the particles, and $V(\mathbf{x})$ is the trapping potential.

A serious obstacle in the study of BEC in atomic systems is the extremely low temperatures required to create the condensate. Because of this difficulty, other, non-

atomic systems are being explored that can undergo condensation at higher temperatures. One possible candidate is a system of exciton–polaritons, which are quasiparticles that can be created in semiconductor cavities as a result of interaction between excitons and a laser field in the cavity (Kasprzak et al. 2006; Coldren and Corzine 1995). A two-dimensional quantum structure consisting of coupled quantum wells embedded in an optical microcavity is used (see Fig. 1). Excitons are electron–hole pairs, produced in the coupled quantum wells, that interact with the photons trapped inside the optical cavity by means of two highly reflective mirrors. Due to this confinement, the effective mass of the polaritons is very small: 10^{-4} times the free-electron mass (Kasprzak et al. 2006). Since the temperature of condensation is inversely proportional to the mass of the particles, the exciton–polariton systems afford relatively high temperatures of condensation. There are, however, two drawbacks in this new condensate: The polaritons are highly unstable and exhibit strong interactions. The excitons disappear with the recombination of the electron–hole pairs through emission of photons. One way to deal with this problem is to introduce a polariton reservoir: Polaritons are "cooled" and "pumped" from this reservoir into the condensate to compensate for the decay. At the same time, a low-density level is kept in order to reduce the interactions between polaritons. For a detailed study of this system, see, e.g., (Bramati and Modugno 2013; Borgh et al. 2012; Keeling and Berloff 2011).

Various mathematical models have been proposed for this new condensate (Keeling and Berloff 2008; Sanvitto et al. 2010; Wouters and Carusotto 2007). One of them, called complex GP equation (Keeling and Berloff 2008), is explored in this paper. The complex GP equation reflects the non-equilibrium dynamics described above by adding pumping and decaying terms to the GP equation. In Keeling and Berloff (2008), the authors observed the formation of two-dimensional vortex lattices. Linear stability of stationary solutions and the formation of dark solitons in the one-dimensional complex GP equation were analyzed by Cuevas et al. (2011). The role of damping in the absence of the pumping term in the GP equation is studied by, e.g., Bao et al. (2004) and Antonelli et al. (2013).

The remainder of the paper is organized as follows. In Sect. 2, the stationary radial solutions of the complex GP equation are calculated. In Sect. 3, a numerical collocation method is used to compute the solutions described in Sect. 2. In Sect. 4, the linear

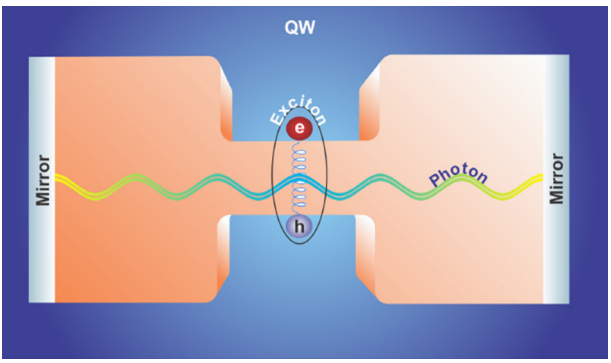

Fig. 1 Schematics of the exciton–polariton microcavity

stability of the stationary states is analyzed. In Sect. 5, the numerical continuation of one of the linearly stable solutions is carried out, showing some of the excited states. In Sect. 6, the full complex GP equation is solved numerically by a second-order time-splitting spectral method. Conclusions are drawn in Sect. 7.

2 Stationary Radial Solutions

Let us analyze solutions of (1) of the form $\psi(x,t) = \exp(-i\mu t)\,\phi(x)$, where μ corresponds to the real-valued chemical potential and ϕ represents the amplitude function that vanishes as $|x| \to \infty$. Introducing this ansatz into (1) leads to the following equation for ϕ,

$$\mu\phi(x) = \left[-\Delta + V(x) + |\phi(x)|^2 + i\left(\omega(x) - \sigma|\phi(x)|^2\right)\right]\phi(x). \tag{3}$$

Multiplying (3) by ϕ^* (the complex conjugate of ϕ) and integrating over $D = \mathbb{R}^2$ yield

$$\mu\int_D |\phi(x)|^2\,\mathrm{d}x = \int_D \Big[|\nabla\phi(x)|^2 + V(x)|\phi(x)|^2 + |\phi(x)|^4 + i\left(\omega(x) - \sigma|\phi(x)|^2\right)|\phi(x)|^2\Big]\mathrm{d}x. \tag{4}$$

It follows immediately that, for μ to be real, it must be required that

$$\int_D \left(\omega(x) - \sigma|\phi(x)|^2\right)|\phi(x)|^2\,\mathrm{d}x = 0. \tag{5}$$

Note that allowing $\mathrm{Im}(\mu) \neq 0$ would lead to exponential growth ($\mathrm{Im}(\mu) > 0$) or exponential decay to zero ($\mathrm{Im}(\mu) < 0$) of the solution, since in this case $\psi(x,t) = \exp(-i\mathrm{Re}(\mu)t)\exp(\mathrm{Im}(\mu)t)\,\phi(x)$.

An alternative approach to study the stationary solutions of (1) is given by its quantum hydrodynamic version. For this, define $S = S(x,t)$ as the phase of ψ and $\rho = \rho(x,t) = |\psi(x,t)|^2$. Hence, inserting the ansatz $\psi = \sqrt{\rho}\exp(iS)$ into (1) and separating real and imaginary parts yield

$$\frac{1}{2}\rho_t + \mathrm{div}J - (\omega(x) - \sigma\rho)\rho = 0, \tag{6}$$

$$S_t + |\nabla S|^2 + V - \frac{\triangle\sqrt{\rho}}{\sqrt{\rho}} + \rho = 0, \tag{7}$$

where $J = J(x,t) = \mathrm{Im}(\psi^*\nabla\psi)$ is the current density. Taking the gradient of (7), multiplying by ρ, and using (6) and $\mathrm{div}(J\otimes J/\rho) = \frac{1}{2}\rho\nabla|\nabla S|^2 + \nabla S\cdot\mathrm{div}J$ give the following equivalent expression of (7):

$$J_t + 2\mathrm{div}\left(\frac{J\otimes J}{\rho}\right) + \rho\nabla V - \rho\nabla\left(\frac{\triangle\sqrt{\rho}}{\sqrt{\rho}}\right) + \frac{1}{2}\nabla\rho^2 = 2(\omega(x) - \sigma\rho)J. \tag{8}$$

Gasser and Markowich (1997) showed that each of the terms in (8), in particular the nonlinear terms with singularities in the vacuum state ($\rho \equiv 0$), is well defined in the sense of distributions if finite kinetic energy solutions are considered, i.e.,

$$\int_D |\nabla \psi|^2 \, \mathrm{d}x < \infty.$$

Using this result, the next theorem can be deduced from (6) and (8).

Theorem 1 *Let $\omega = \omega(x) \geq 0$ be smooth with $\{x | \omega(x) > 0\}$ simply connected. Then, there exists a stationary solution of (6)–(8) with $J \equiv 0$ if and only if either*

1. *$\rho \equiv 0$, or*
2. *$\rho = \frac{\omega(x)}{\sigma}$. In this case, $V(x) = C + \frac{\triangle\sqrt{\omega(x)}}{\sqrt{\omega(x)}} - \frac{1}{\sigma}\omega(x)$ in $\{x | \omega(x) > 0\}$, where C is a constant.*

Proof Set $\rho_t \equiv 0$, $J_t \equiv 0$, and $J \equiv 0$ in (6) and (8). Then, statement 1 is a trivial solution of the system. For statement 2, notice that (6) yields $\rho = \omega(x)/\sigma$. Inserting this expression into (8) gives

$$\nabla \left(V(x) - \frac{\triangle\sqrt{\omega(x)}}{\sqrt{\omega(x)}} + \frac{1}{\sigma}\omega \right) = 0, \quad \text{in } \{x | \omega(x) > 0\}.$$

Hence,

$$V(x) = C + \frac{\triangle\sqrt{\omega(x)}}{\sqrt{\omega(x)}} - \frac{1}{\sigma}\omega, \quad \text{in } \{x | \omega(x) > 0\}, \tag{9}$$

where C is a constant.

Now, if statement 1 is true, then $J \equiv 0$ follows immediately. On the other hand, if statement 2 is valid, then (7) gives $|\nabla S|^2 = 0$, which implies $\nabla S = 0$. Thus, $J (= \rho \nabla S) \equiv 0$.

Remark 2 The stationary GP equation,

$$V(x) = \mu + \frac{\triangle\phi}{\phi} - \frac{1}{\sigma}|\phi|^2, \quad \phi \neq 0, \tag{10}$$

has exactly the form of (9), with $C = \mu$ (the chemical potential). Then, letting $\omega(x) = |\phi|^2$ [the density profile of any solution of (10)], the solution of the corresponding complex GP equation is given by $\rho = |\phi|^2/\sigma$ with $J \equiv 0$.

Now, going back to (6) and integrating in space give

$$\frac{1}{2}\frac{\mathrm{d}M}{\mathrm{d}t} = \int_D (\omega(x) - \sigma\rho)\rho \mathrm{d}x,$$

where

$$M \equiv \int_D \rho \mathrm{d}x$$

is the *mass* of the system. Therefore, we can see that equation (3) along with condition (5) leads to solutions where the pumping and decaying parts equilibrate, i.e., the time derivative of the mass of the system is zero. In addition, condition (5) ensures that the chemical potential is a nonnegative real quantity.

For the rest of the paper, $V(x) = |x|^2$ is the harmonic potential and $\omega(x) = \alpha\Theta(R - |x|)$, where $\alpha > 0$ is the strength of the pumping term and $R > 0$ is the radius of the pumping region delimited by the smoothed Heaviside function $\Theta(x) = (1 + \tanh(\kappa x))/2$ for some fixed parameter $\kappa > 0$.

In the following, we investigate the stationary radially symmetric solutions of (3). In this case, (3) becomes ($' = \frac{\mathrm{d}}{\mathrm{d}r}$, $\Theta_R = \Theta(R - r)$)

$$\mu\phi = -\phi'' - \frac{1}{r}\phi' + r^2\phi + |\phi|^2\phi + i\left(\alpha\Theta_R - \sigma|\phi|^2\right)\phi, \tag{11}$$

where $r = |x| \geq 0$, with the boundary conditions $\phi(r) = 0$ as $r \to \infty$ and $\phi'(0) = 0$. Condition (5) is written as

$$\int_0^\infty \left(\alpha\Theta_R - \sigma|\phi(r)|^2\right)|\phi(r)|^2 r\mathrm{d}r = 0. \tag{12}$$

By defining

$$\xi(r) = \int_0^r \left(\alpha\Theta_R - \sigma|\phi(s)|^2\right)|\phi(s)|^2 s\mathrm{d}s, \tag{13}$$

condition (12) can be expressed as

$$\xi'(r) = \left(\alpha\Theta_R - \sigma|\phi(r)|^2\right)|\phi(r)|^2 r, \tag{14}$$

with

$$\xi(\infty) = 0. \tag{15}$$

The variable ξ is convenient for subsequent numerical integration. The constancy of the chemical potential μ can be written as

$$\mu'(r) = 0. \tag{16}$$

Because the phase of ϕ is arbitrary, we let

$$\mathrm{Im}(\phi(0)) = 0. \tag{17}$$

Notice that the second-order ordinary differential equation (ODE) (11) can be expanded as a system of two first-order ODE. Due to the harmonic trapping potential and the finite pumping region, the solution is expected to be concentrated on a bounded domain. This fact is used in the numerical computations, where the integration domain is chosen as $D = [0, b]$ for large enough b. Then, the right boundary conditions, $\phi(\infty) = 0$ and $\xi(\infty) = 0$, are replaced by $\phi(b) = 0$ and $\xi(b) = 0$, respectively. As a result, the following set of ODE is obtained for $r \in [0, b]$:

$$\begin{aligned}
\phi' &= \varphi, \\
\varphi' &= -\frac{1}{r}\varphi - \mu\phi + r^2\phi + |\phi|^2\phi + i\left(\alpha\Theta_R - \sigma|\phi|^2\right)\phi, \\
\xi' &= \left(\alpha\Theta_R - \sigma|\phi(r)|^2\right)|\phi(r)|^2 r, \\
\mu' &= 0,
\end{aligned} \tag{18}$$

with

$$\phi(b) = 0, \quad \varphi(0) = 0, \quad \mathrm{Im}(\phi(0)) = 0, \quad \xi(b) = 0.$$

This nonlinear boundary value problem with a singularity of the first kind (see, e.g., Hoog and Weiss 1976) is consistent with respect to the number of boundary conditions. The value of φ' at $r = 0$ can be determined using

$$\lim_{r\to 0}\frac{\varphi(r) - \varphi(0)}{r - 0} = \lim_{r\to 0}\frac{\varphi(r)}{r} = \varphi_r(0), \tag{19}$$

due to the boundary condition $\varphi(0) = 0$. Then, the second equation in (18) gives

$$\varphi'(0) = \frac{1}{2}\left[-\mu\phi(0) + |\phi(0)|^2\phi(0) + i\left(\alpha - \sigma|\phi(0)|^2\right)\phi(0)\right]. \tag{20}$$

It is convenient to make (18) real valued, autonomous, and restricted to the interval $[0, 1]$. Substituting $\phi = \theta + i\eta$ into (11), separating real and imaginary parts, and writing the resulting equations as a system of first-order ODE lead to a real-valued system. In order to make (18) autonomous, define $\varrho(r) = r$ such that $\varrho'(r) = 1$ and $\varrho(0) = 0$ are added to the system. Finally, rescaling r as $\tilde{r} = \frac{r}{b}$ restricts the domain to the interval $[0, 1]$. Thus, (18) becomes ($' = \frac{\mathrm{d}}{\mathrm{d}\tilde{r}}$):

$$\begin{aligned}
\frac{1}{b}\theta' &= \varphi, \\
\frac{1}{b}\varphi' &= -\frac{1}{\varrho}\varphi - \mu\theta + \varrho^2\theta + \left(\theta^2 + \eta^2\right)\theta - \left(\alpha\Theta(R - \varrho) - \sigma\left(\theta^2 + \eta^2\right)\right)\eta, \\
\frac{1}{b}\eta' &= \zeta, \\
\frac{1}{b}\zeta' &= -\frac{1}{\varrho}\zeta - \mu\eta + \varrho^2\eta + \left(\theta^2 + \eta^2\right)\eta + \left(\alpha\Theta(R - \varrho) - \sigma\left(\theta^2 + \eta^2\right)\right)\theta,
\end{aligned}$$

$$\begin{aligned}
\frac{1}{b}\xi' &= \left(\alpha\Theta\left(R-\varrho\right)-\sigma\left(\theta^2+\eta^2\right)\right)\left(\theta^2+\eta^2\right)\varrho,\\
\frac{1}{b}\mu' &= 0,\\
\frac{1}{b}\varrho' &= 1,
\end{aligned} \tag{21}$$

with

$$\varphi\left(0\right)=0,\quad \theta\left(1\right)=0,\quad \zeta\left(0\right)=0,\quad \eta\left(0\right)=0,\quad \eta\left(1\right)=0,\quad \xi\left(1\right)=0,\quad \varrho\left(0\right)=0.$$

3 Collocation Method

System (21) can be solved with high accuracy by using a collocation method. The basic idea involves forming an approximate solution as a linear combination of a set of functions (usually polynomials), the coefficients of which are determined by requiring the combination to satisfy the system at certain points (the collocation points) as well as the boundary conditions.

To introduce the algorithm, consider the following first-order system of ODE:

$$u'\left(r\right)=f\left(u\left(r\right)\right),\quad r\in I=\left[0,1\right],\quad u\left(\cdot\right),f\left(\cdot\right)\in\mathbb{R}^d, \tag{22}$$

subject to the boundary conditions

$$b\left(u\left(0\right),u\left(1\right)\right)=0,\quad b\left(\cdot\right)\in\mathbb{R}^d.$$

Let $I_h=\{r_n:0=r_0<r_1<\cdots<r_N=1\}$ be a given mesh on I, with $h_n=r_n-r_{n-1}$ $(n=1,\ldots,N)$. Define the space of vector-valued piecewise polynomials, $\mathcal{P}^m\left(I_h\right)$, as

$$\mathcal{P}^m\left(I_h\right)=\left\{v\in C\left(I\right):\ v\mid_{[r_{n-1},r_n]}\in\pi_m,\ \left(1\le n\le N\right)\right\},$$

where π_m is the space of all vector-valued polynomials of degree $\le m$. The collocation method consists of finding an element $q_h\in\mathcal{P}^m\left(I_h\right)$ that approximates the solution of (22). Such approximation will be found by requiring q_h to satisfy (22) on a given finite subset, S_h, of I, as well as the boundary conditions.

Let S_h, the set of collocation points, be given by

$$S_h=\left\{r_{n,i}=r_{n-1}+c_ih_n:\ 1\le n\le N,\ 0=c_1<c_2<\cdots<c_m=1\right\},$$

where $\{c_i\}$ are usually Gauss, Radau, or Lobatto points (see, e.g., Ascher et al. 1987). The collocation solution $q_h\in\mathcal{P}^m\left(I_h\right)$ for (22) is defined by the equation

$$q_h'\left(r_{n,i}\right)=f\left(q_h\left(r_{n,i}\right)\right),\quad r_{n,i}\in S_h,\quad b\left(q_h\left(0\right),q_h\left(1\right)\right)=0.$$

Now, consider a local Lagrange basis representation of q_h. Define

$$L_i(\delta) := \prod_{k=1,k\neq i}^{m} \frac{\delta - c_k}{c_i - c_k}, \quad (i = 1, \ldots, m), \quad \delta \in [0,1].$$

Then, the local polynomials can be written as

$$q_n(r_{n-1} + \delta h_n) = \sum_{i=1}^{m} L_i(\delta)\, q_h(r_{n-1} + c_i h_n), \; 1 \le n \le N, \quad \delta \in [0,1].$$

The collocation equations are, therefore,

$$q_n'(r_{n,i}) = f(q_n(r_{n,i})), \quad r_{n,i} \in S_h, \quad 1 \le n \le N, \tag{23}$$

with the boundary conditions

$$b_l(u_0, u_N) = 0, \quad l = 1, \ldots, d. \tag{24}$$

Equations (23)–(24) can be solved by a Newton–Chord iteration. It can be proven that if the solution $u(r)$ of the boundary value problem is sufficiently smooth, then the order of accuracy of the method is m, i.e., $\|q_h - u\|_\infty = \mathcal{O}(h^m)$, where $h := \max\{h_n : 1 \le n \le N\}$ (the diameter of the mesh I_h). For a detailed description of this method, the reader is referred to Ascher et al. (1987) and Brunner (2004).

The MATLAB function *bvp5c* is used to solve system (21) by the collocation method. This function implements a four-point Lobatto method capable of handling singularities of the first kind and mesh adaptation. In addition, *bvp5c* can converge even if the initial guess is not very close to the solution; that is, the function converges by using as an initial guess the Thomas–Fermi profile (Keeling and Berloff 2008):

$$|\phi|^2 = \begin{cases} \tilde{\mu} - r^2, & r < \sqrt{\tilde{\mu}}, \\ 0, & r \ge \sqrt{\tilde{\mu}}, \end{cases} \quad \tilde{\mu} = 3\alpha/2\sigma. \tag{25}$$

It is important to note that *bvp5c* always evaluates the ODE at the end points. Then, due to the singularity, the value obtained in (20) must be supplied to *bvp5c* when evaluating the ODE at $r = 0$.

With 6000 grid points (initially equispaced) on the domain $D = [0, 15]$, the maximum residual obtained is less than 10^{-11} for the different cases studied: $\alpha = 4.4$, $\sigma = 0.3$, $\kappa = 10$, and $0 < R < 10$. In the following section, a linear stability analysis is performed on these results, which are later used as a starting point in the numerical continuation.

4 Linear Stability Analysis of the Radially Symmetric Solutions

Consider the radially symmetric solutions $\psi(r,t) = \exp(-i\mu t)\,\phi(r)$ obtained in the previous section. To study their linear stability, small perturbations of the wave function can be expressed as

$$\psi(r,\theta,t) = \exp(-i\mu t)\left[\phi(r) + \varepsilon\left(u(r)\exp\left(-i\left(m\theta+\omega t\right)\right)\right.\right.$$
$$\left.\left. + v^*(r)\exp\left(i\left(m\theta+\omega^* t\right)\right)\right)\right], \tag{26}$$

with $\varepsilon \ll 1$, $m = 1, 2, 3, \ldots$

This form of the perturbation and the subsequent calculations are known as Bogoliubov–De Gennes analysis. Notice that the perturbation is time dependent with frequency ω and complex amplitude functions $u(r)$ and $v(r)$. In addition, the perturbation is both radial and angular, where the angular part is tested with different modes given by m. The radially symmetric solutions are linearly unstable if $\mathrm{Im}(\omega) > 0$.

We proceed by evaluating the complex GP equation for the trial wave function (26) to $\mathcal{O}(\varepsilon)$. To simplify the notation, we write $\phi(r)$, $u(r)$, and $v(r)$ as ϕ, u, and v, respectively. Equating terms in $\exp(-i\mu t)$ yields the equation for the radially symmetric solutions:

$$\mu\phi = \left(-\frac{\mathrm{d}^2}{\mathrm{d}r^2} - \frac{1}{r}\frac{\mathrm{d}}{\mathrm{d}r} + r^2 + |\phi|^2 + i\left(\alpha\Theta_R - \sigma|\phi|^2\right)\right)\phi. \tag{27}$$

Equating terms in $\exp(-i(m\theta + (\mu+\omega)t))$ leads to

$$(\mu+\omega)u = \left(-\frac{\mathrm{d}^2}{\mathrm{d}r^2} - \frac{1}{r}\frac{\mathrm{d}}{\mathrm{d}r} + \frac{m^2}{r^2} + r^2 + 2|\phi|^2\right.$$
$$\left. + i\left(\alpha\Theta_R - 2\sigma|\phi|^2\right)\right)u + (1-i\sigma)\phi^2 v. \tag{28}$$

Equating terms in $\exp(i(m\theta - (\mu-\omega^*)t))$ gives

$$\left(\mu-\omega^*\right)v^* = \left(-\frac{\mathrm{d}^2}{\mathrm{d}r^2} - \frac{1}{r}\frac{\mathrm{d}}{\mathrm{d}r} + \frac{m^2}{r^2} + r^2 + 2|\phi|^2\right.$$
$$\left. + i\left(\alpha\Theta_R - 2\sigma|\phi|^2\right)\right)v^* + (1-i\sigma)\phi^2 u^*. \tag{29}$$

Taking the complex conjugate of (29) produces

$$(\mu-\omega)v = \left(-\frac{\mathrm{d}^2}{\mathrm{d}r^2} - \frac{1}{r}\frac{\mathrm{d}}{\mathrm{d}r} + \frac{m^2}{r^2} + r^2 + 2|\phi|^2\right.$$
$$\left. - i\left(\alpha\Theta_R - 2\sigma|\phi|^2\right)\right)v + (1+i\sigma)\left(\phi^*\right)^2 u. \tag{30}$$

Finally, Eqs. (28) and (30) can be written as

$$\begin{bmatrix} L_1 & L_2 \\ -L_2^* & -L_1^* \end{bmatrix}\begin{bmatrix} u \\ v \end{bmatrix} = \omega\begin{bmatrix} u \\ v \end{bmatrix}, \tag{31}$$

with

$$L_1 = -\mu - \frac{\mathrm{d}^2}{\mathrm{d}r^2} - \frac{1}{r}\frac{\mathrm{d}}{\mathrm{d}r} + \frac{m^2}{r^2} + r^2 + 2|\phi|^2 + i\left(\alpha\Theta_R - 2\sigma|\phi|^2\right)$$
$$= -\mu - \frac{\mathrm{d}^2}{\mathrm{d}r^2} - \frac{1}{r}\frac{\mathrm{d}}{\mathrm{d}r} + \frac{m^2}{r^2} + r^2 + 2(1-i\sigma)|\phi|^2 + i\alpha\Theta_R,$$

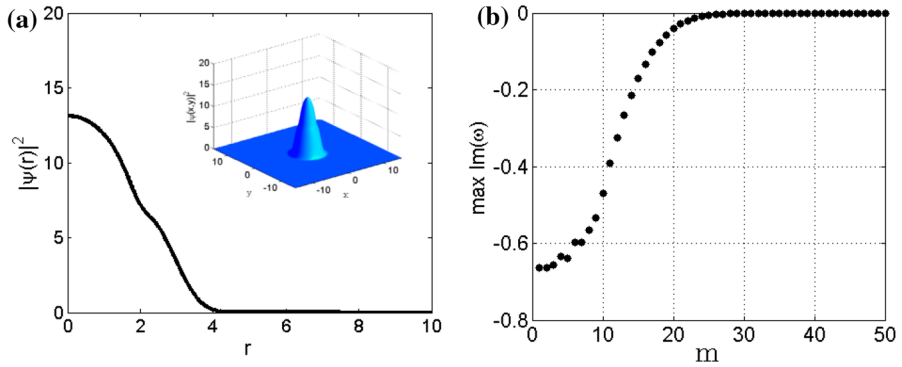

Fig. 2 **a** Density profile of the radially symmetric solution for $R = 2$, with the two-dimensional view shown in the *inset*. **b** Results from the linear stability analysis: The plot shows the maximum imaginary part of the eigenvalues, ω, for $m = 1, 2, \ldots, 50$

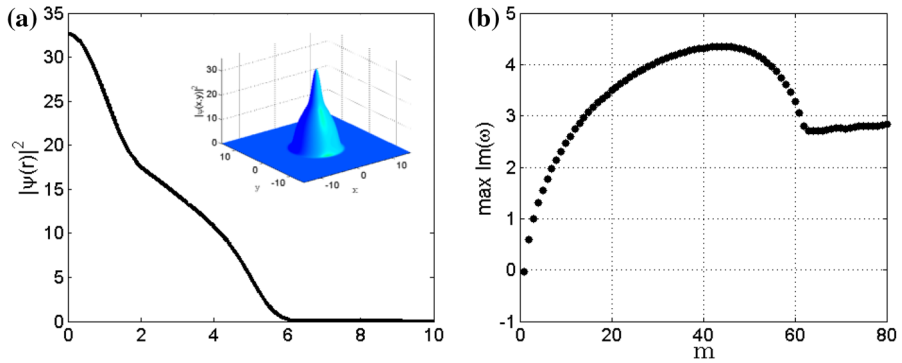

Fig. 3 **a** Density profile of the radially symmetric solution for $R = 8$, with the two-dimensional view shown in the *inset*. **b** Results from the linear stability analysis: The plot shows the maximum imaginary part of the eigenvalues, ω, for $m = 1, 2, \ldots, 80$

and

$$L_2 = (1 - i\sigma)\,\phi^2.$$

The eigenvalue problem (31) is discretized by using centered differences and solved with the MATLAB function eig. The results for $R = 2$ are plotted in Fig. 2. Figure 2b shows the maximum imaginary part of the eigenvalues, ω, for $m = 1, 2, \ldots, 50$. Notice that all of them are negative; thus, the solution is linearly stable under these perturbations. Taking this into account, this solution will be used as a starting point in the numerical continuation method presented in the following section.

Figures 3 and 4 show two cases where the solutions are linearly unstable. An interesting observation is the fact that the radially symmetric solutions are the same for large enough values of R; we note that this is the case for $R = 8$ and $R = 9$. This characteristic was also observed by Cuevas et al. (2011) for the one-dimensional complex GP equation.

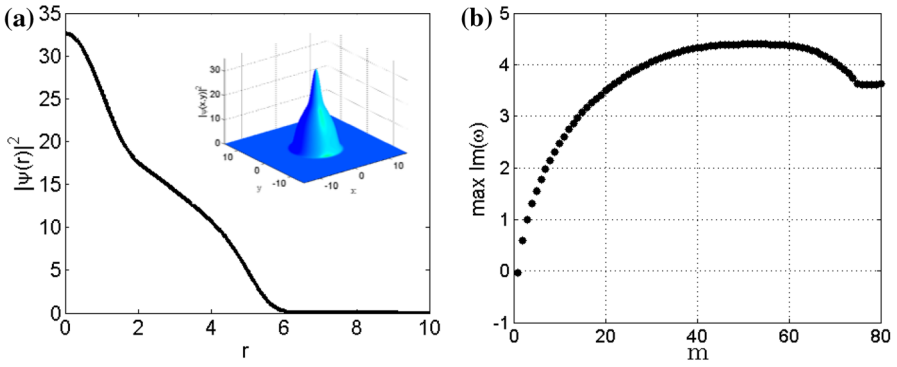

Fig. 4 **a** Density profile of the radially symmetric solution for $R = 9$, with the two-dimensional view shown in the *inset*. **b** Results from the linear stability analysis: The plot shows the maximum imaginary part of the eigenvalues, ω, for $m = 1, 2, \ldots, 80$

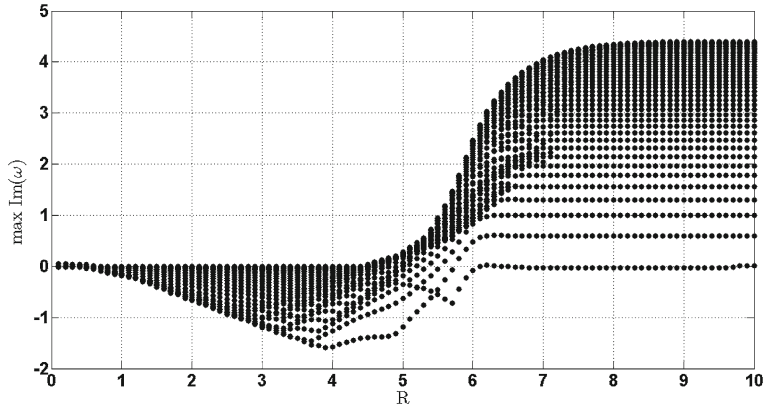

Fig. 5 Results for $0 < R < 10$ (with spacing of 0.1) showing the maximum imaginary part of the eigenvalues, ω, for $m = 1, 2, \ldots, 50$. Instability for this particular branch exists at both $R \lesssim 0.6$ and $R \gtrsim 4.4$

Figure 5 shows the maximum imaginary part of the eigenvalues, ω, for $0 < R < 10$, with spacing of 0.1 in R and for $m = 1, 2, \ldots, 50$. Notice that for large values of R, which in this case also implies large mass, the solutions become unstable. However, the solutions are seen to be also unstable for small values of R (small mass), i.e., at $R \lesssim 0.6$. For $R \lesssim 0.6$, it was observed that a different branch of solutions with smaller chemical potential, μ, becomes stable. The case of large values of R is studied in detail in Sect. 6. Finally, Fig. 6 shows the magnitude of the current, $|J|$, corresponding to the solutions for $R = 2, 8, 9$.

The instabilities closely related to those discussed in this section have been observed in various experiments on polariton condensates (see, e.g., Manni et al. 2011; Ohadi et al. 2012). Amo et al. (2009) point out that as the pumping intensity increases (represented here by α in the complex GP equation), polariton–polariton interactions become stronger, resulting in higher polariton dispersion and instabilities. This effect is some-

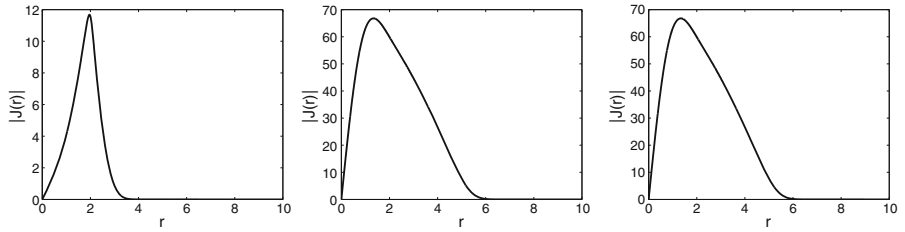

Fig. 6 Magnitude of the current, J, corresponding to the solutions for $R = 2$ (*left*), $R = 8$ (*center*), and $R = 9$ (*right*)

what similar to the increase of the pumping region analyzed in this section, where we observe that the radially symmetric solutions become less stable as R increases. Furthermore, Ballarini et al. (2009) have observed long-lived polariton states across a parametric threshold of the pumping intensity, which is also similar to our results for small values of R. We must emphasize that the fact that the solution branch analyzed in this section becomes unstable for R small does not mean that no radially symmetric stable solution exists for these parameters. In the following section, we show the complicated interaction of the different branches of solutions for the radially symmetric stationary complex GP equation. In this case, a different branch becomes stable for small values of R, as mentioned before. There is no pattern formation, but rather a transition from the unstable radially symmetric branch to another, stable, radially symmetric branch. This is also something important to consider when studying the complex GP equation: It is not easy to define a ground-state solution for this equation due to the intrinsic non-equilibrium dynamics that it describes. This is reflected in the fact that the energy cannot be globally conserved as in the case of the GP equation. Hence, a direct study of the stationary GP equation is necessary. But in this case, we have to be careful because we cannot expect uniqueness of solutions for this equation, and additional criteria must be considered to define a ground-state solution.

5 Numerical Continuation for the Stationary Solutions

Let us rewrite system (21) as

$$F(u, \lambda) = 0, \tag{32}$$

where u is the solution of the system ($u \in \mathcal{B}$, a real Banach space), λ is a real parameter (λ can be α, σ, or R), and F is a continuously differentiable operator such that $F : \mathcal{B} \times \mathbb{R} \to \mathcal{B}$. The idea in this section is to study the dependence of the solution, $u(\lambda)$, on the parameter, λ, i.e., to trace the solution branches $[u(\lambda), \lambda]$ of (32). Since the operator F is nonlinear in u and λ, this can be performed numerically by Newton's method: Suppose that (u_0, λ_0) is a solution of the discretized problem (32) and that the directional derivative $\dot{u}_0 = du_0/d\lambda$ is known. Then, the solution u_1 at $\lambda_1 = \lambda_0 + \Delta\lambda$ (where Δ represents a small increment) can be computed as

$$\begin{cases} F_u\left(u_1^i, \lambda_1\right) \Delta u_1^i = -F\left(u_1^i, \lambda_1\right), \\ u_1^{i+1} = u_1^i + \Delta u_1^i, \quad i = 0, 1, 2, \ldots \end{cases}$$

with

$$u_1^0 = u_0 + \Delta\lambda \dot{u}_0,$$

where $F_u\left(u, \lambda\right)$ is the Jacobian matrix.

This method, however, is unable to handle the continuation near singular points known as turning points or folds, where the solution branch bends back on itself and $F_u\left(u, \lambda\right)$ becomes singular. These points are particularly important to study the excited states of the complex GP equation.

A pseudo-arclength continuation method can be used to overcome this problem. The main difference from the previous algorithm is the parametrization of the solution in terms of a new quantity, ν, that approximates the arclength, s, in the tangent space of the curve (instead of the parametrization by λ). This is usually accomplished by appending an auxiliary equation to (32) that approximates the arclength condition

$$\left\|\dot{u}\left(s\right)\right\|^2 + \left|\dot{\lambda}\left(s\right)\right|^2 = 1. \tag{33}$$

This leads to the augmented system

$$\begin{cases} F\left(u\left(\nu\right), \lambda\left(\nu\right)\right) = 0, \\ N\left(u\left(\nu\right), \lambda\left(\nu\right), \nu\right) = 0, \end{cases} \tag{34}$$

with unknowns $u\left(\nu\right)$ and $\lambda\left(\nu\right)$. Then, Newton's method (or one of its variants) can be used to solve (34), in which case the Jacobian of the system becomes the bordered matrix:

$$G = \begin{bmatrix} F_u & F_\lambda \\ N_u & N_\lambda \end{bmatrix}.$$

For a detailed description of bordered matrices, see, e.g., Govaerts (2000). The function N is defined such that the Jacobian G is non-singular on the solution branch, including turning points and their neighborhoods. $N\left(u, \lambda, \nu\right) \equiv \dot{u}_0^T\left(u - u_0\right) + \dot{\lambda}_0\left(\lambda - \lambda_0\right) - \nu$ is one of the most frequently used definitions of N. It was introduced by Keller (1977). With this particular definition of N, the method is known as Keller's algorithm.

The pseudo-arclength continuation method can be summarized as follows: The unit tangent $\left(\dot{u}_0, \dot{\lambda}_0\right)$ at $\left(u_0, \lambda_0\right)$ is obtained from its definition:

$$\begin{cases} F_u\left(u_0, \lambda_0\right) \dot{u}_0 + F_\lambda\left(u_0, \lambda_0\right) \dot{\lambda}_0 = 0, \\ \left\|\dot{u}_0\right\|^2 + \left|\dot{\lambda}_0\right|^2 = 1. \end{cases}$$

Then, an approximate solution $\left(u_a, \lambda_a\right)$ is computed as

$$\begin{aligned} u_a &= u_0 + \nu \dot{u}_0, \\ \lambda_a &= \lambda_0 + \nu \dot{\lambda}_0, \end{aligned}$$

which is used as an initial guess in a Newton-like method for solving (34) to obtain $(u(\nu), \lambda(\nu))$.

The software package AUTO Doedel et al. (2007) was used for the continuation of the two-dimensional radially symmetric solutions of the complex GP equation. AUTO implements Keller's pseudo-arclength continuation algorithm. A detailed description of this algorithm can be found in Keller (1987). In addition to detecting turning points, AUTO can also find branch points, a feature that will be used to study the excited states of the complex GP equation.

AUTO discretizes system (21) using polynomial collocation with Gaussian points. The number of free parameters, p, controlled by AUTO during the continuation process is given by $p = n_{bc} + 1 - n$, where n_{bc} is the number of boundary conditions and n is the dimension of the system. Hence, the continuation for system (21) can be done in one parameter. For the results presented in this section, the number of mesh intervals is 6000, the number of Gaussian collocation points per mesh interval is 7, and the maximum absolute value of the pseudo-arclength stepsize is 0.0001. The parallel version of AUTO was run on a Beowulf-class heterogeneous computer cluster using 16 nodes for a total of 128 cores (Intel Xeon X5570, 2.93GHz).

Figure 7 shows the chemical potential, μ, of the different solutions obtained by the continuation in σ with $\alpha = 4.4$ and $R = 2$ fixed. By using different initial guesses (multi-bump profiles) in the collocation method described in Sect. 3, it was possible to find some of the solutions shown in Figs. 8 and 9. These solutions, along with the capability of AUTO to detect branch points and turning points, were employed to produce the result displayed in Fig. 7. In this figure, the red dashed line indicates the solutions corresponding to $\sigma = 0.3$, $\alpha = 4.4$ and $R = 2$. Figures 8 and 9 show the density profiles of these solutions. Notice that the linearly stable solution studied in Sect. 4 has the smallest chemical potential. In this context, this solution can be considered as the ground-state solution, whereas the other solutions are excited states. In any case, an appropriate definition of the energy for this equation is necessary to determine a ground-state solution. From the numerical results obtained up to now, we expect that the solution labeled 0 in Figs. 7 and 8 is the minimizer of such energy.

Equation (4) can also be used for the computation of the chemical potential. In this case,

$$\mu \int_0^b |\phi(r)|^2 r\,\mathrm{d}r = \int_0^b \left[|\phi'(r)|^2 + r^2 |\phi(r)|^2 + |\phi(r)|^4 \right] r\,\mathrm{d}r, \tag{35}$$

where the integration domain is $[0, b]$. Using Simpson's rule, this expression was used for a second validation of the results presented in Fig. 7.

6 Numerical Integration of the Complex GP Equation

In this section, the numerical integration of the complex GP equation is carried out by using a Strang-splitting Fourier spectral method. This method was studied by Bao et al. (2002) for the Schrödinger equation in the semiclassical regime and by Bao et al. (2003) for the GP equation. For simplicity of notation, the method is presented in one dimension. The generalization to higher dimensions is straightforward using the tensor product grids. The problem can be stated as

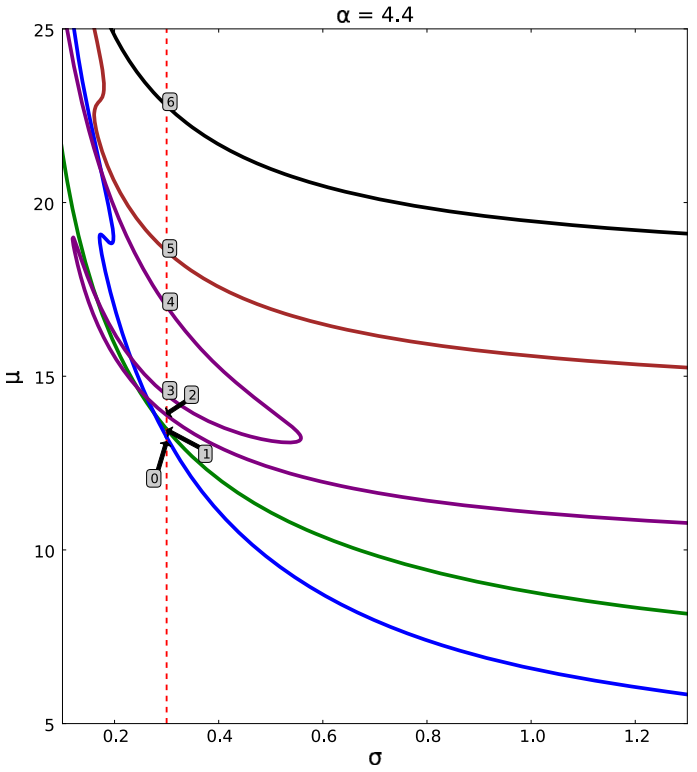

Fig. 7 Results from the continuation method showing the chemical potential of the system for different values of σ with $\alpha = 4.4$ and $R = 2$ fixed. The *red dashed line* indicates the solutions for $\sigma = 0.3$. Figures 8 and 9 show the density profiles corresponding to these solutions (Color figure online)

$$i\psi_t = -\psi_{xx} + V(x)\psi + |\psi|^2\psi + i\left(\alpha\Theta_R - \sigma|\psi|^2\right)\psi,$$
$$\psi(x,0) = \psi_0(x), \quad a \le x \le b, \quad \psi(a,t) = \psi(b,t), \quad \psi_x(a,t) = \psi_x(b,t), t > 0. \tag{36}$$

Notice that in this case, periodic boundary conditions are specified, which are necessary for the implementation, because the discrete Fourier transform is used in one of the steps. In addition, ψ is concentrated due to the trapping potential and vanishes very quickly as $|x|$ increases, making these boundary conditions a good option provided that the domain of integration is large enough.

Consider $h = \Delta x > 0$ as the mesh size, with $h = (b-a)/M$, where M is an even positive integer. Define $\tau = \Delta t > 0$ as the time step. Let the grid points be $x_j = a + jh$, $j = 0, 1, \ldots, M$, and the time $t_n = n\tau$, $n = 0, 1, 2, \ldots$ Finally, define Ψ_j^n as the numerical approximation of $\psi(x_j, t_n)$. Equation (36) is now separated into

$$i\psi_t = V(x)\psi + |\psi|^2\psi + i\left(\alpha\Theta_R - \sigma|\psi|^2\right)\psi \tag{37}$$

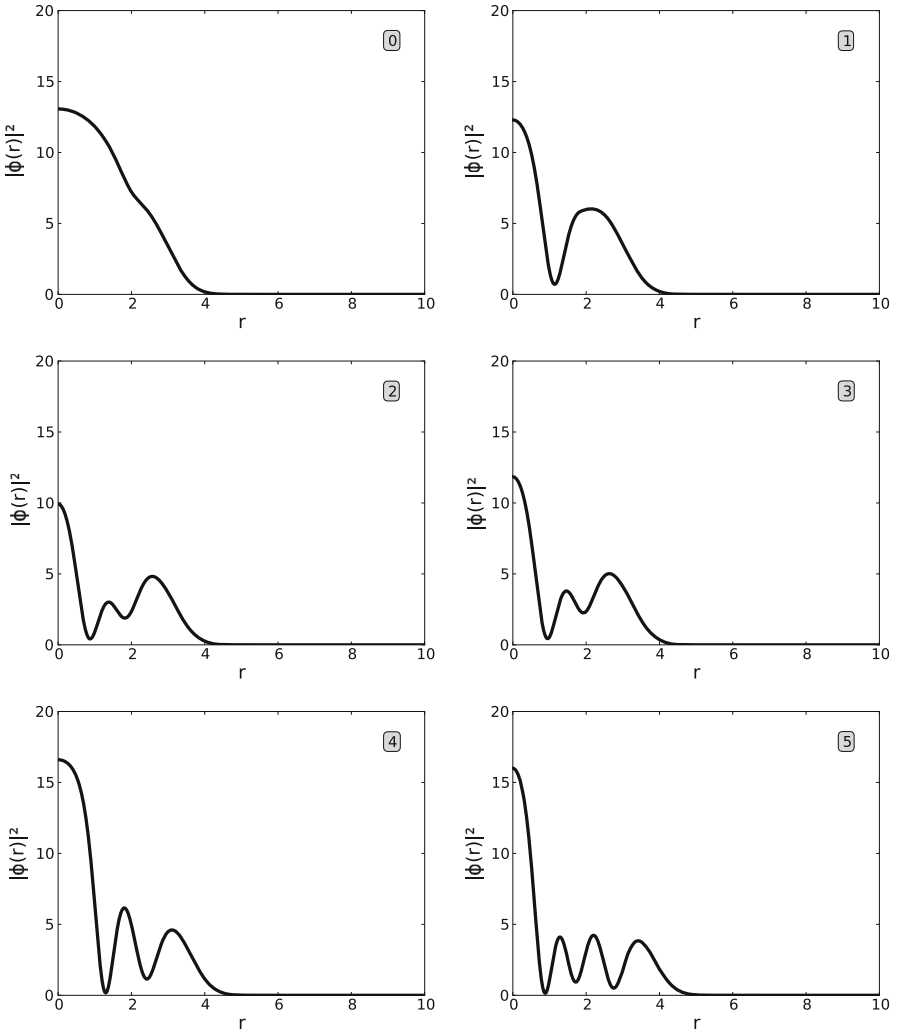

Fig. 8 Density profiles of the solutions labeled 0–5 in Fig. 7

and

$$i\psi_t = -\psi_{xx}, \tag{38}$$

which are combined via Strang splitting to approximate the solution of (36) on $[t_n, t_{n+1}]$.

Step 1 of the Strang-splitting method requires the solution of (37) on a half-time step, from t_n to $t_n + \tau/2$. Due to the smooth Heaviside Θ in (37), two equations are solved: for $\Theta_R > 0$

$$i\psi_t = V(x)\psi + |\psi|^2 \psi + i\left(\alpha\Theta_R - \sigma|\psi|^2\right)\psi, \tag{39}$$

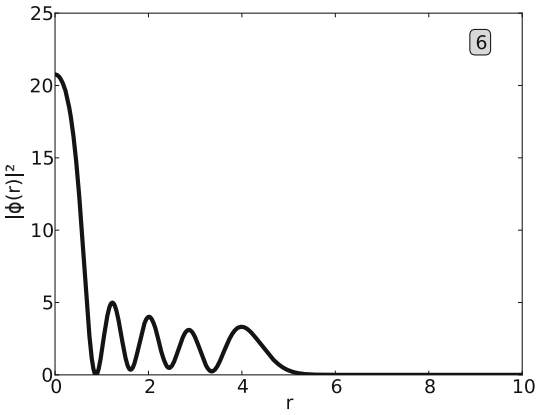

Fig. 9 Density profile of the solution labeled 6 in Fig. 7

and for $\Theta_R = 0$

$$i\psi_t = V(x)\psi + |\psi|^2\psi - i\sigma|\psi|^2\psi. \tag{40}$$

Substituting $\psi(x,t) = \rho(x,t)\, e^{i\theta(x,t)}$ in (39), where ρ is the magnitude and θ is the phase of ψ, gives

$$i\rho_t - \rho\theta_t = V(x)\rho + \rho^3 + i\left(\alpha\Theta_R - \sigma\rho^2\right)\rho. \tag{41}$$

Separating real and imaginary parts from (41) and looking for non-trivial solutions lead to

$$\theta_t = -V(x) - \rho^2, \tag{42}$$

$$\rho_t = \left(\alpha\Theta_R - \sigma\rho^2\right)\rho. \tag{43}$$

The solution of (43) is given by

$$\rho = \sqrt{\frac{\rho_0^2 e^{2\alpha\Theta_R t}}{1 + \frac{\sigma}{\alpha}\rho_0^2\left(e^{2\alpha\Theta_R t} - 1\right)/\Theta_R}},$$

where $\rho_0 = \rho(x,0)$. With this result, (42) can be solved, obtaining

$$\theta = -V(x)t - \frac{1}{2\sigma}\ln\left|1 + \frac{\sigma}{\alpha}\rho_0^2\left(e^{2\alpha\Theta_R t} - 1\right)/\Theta_R\right| + \theta_0,$$

where θ_0 is the phase of the initial condition.

Following the same procedure for (40) yields

$$\rho = \frac{\rho_0}{\sqrt{2\sigma\rho_0^2 t + 1}},$$

$$\theta = -V(x)t - \frac{1}{2\sigma}\ln\left|2\sigma\rho_0^2 t + 1\right| + \theta_0.$$

Hence, defining $\Theta_j \equiv \Theta\left(R - \left|x_j\right|\right)$, the solution of Step 1 can be written as:

$$\Psi_j^{(1)} = \begin{cases} \Psi_j^n U_j^{(1)} e^{i\theta_j^{(1)}}, & \Theta_j > 0, \\ \Psi_j^n W_j^{(1)} e^{i\phi_j^{(1)}}, & \Theta_j = 0, \end{cases}$$

where

$$\begin{aligned} U_j^{(1)} &= \sqrt{\frac{e^{\alpha\Theta_j\tau}}{1 + \frac{\sigma}{\alpha}\left|\Psi_j^n\right|^2\left(e^{\alpha\Theta_j\tau} - 1\right)/\Theta_j}}, \\ \theta_j^{(1)} &= -V(x_j)\tau/2 - \frac{1}{2\sigma}\ln\left|1 + \frac{\sigma}{\alpha}\left|\Psi_j^n\right|^2\left(e^{\alpha\Theta_j\tau} - 1\right)/\Theta_j\right|, \\ W_j^{(1)} &= \frac{1}{\sqrt{\sigma\left|\Psi_j^n\right|^2\tau + 1}}, \\ \phi_j^{(1)} &= -V(x_j)\tau/2 - \frac{1}{2\sigma}\ln\left|\sigma\left|\Psi_j^n\right|^2\tau + 1\right|. \end{aligned}$$

For Step 2, Eq. (38) has to be solved on a complete time step, from t_n to $t_n + \tau$, using the solution of Step 1 as the initial condition. Equation (38) is discretized in space by the Fourier spectral method and integrated in time exactly, giving

$$\Psi_j^{(2)} = \frac{1}{M}\sum_{l=-M/2}^{M/2-1} e^{-i\omega_l^2\tau}\widehat{\Psi}_l^{(1)} e^{i\omega_l(x_j-a)}, \quad j = 0, 1, 2, \ldots, M-1,$$

where $\widehat{\Psi}_l^{(1)}$, the Fourier coefficients of $\Psi^{(1)}$, are defined as

$$\widehat{\Psi}_l^{(1)} = \sum_{j=0}^{M-1}\Psi_j^{(1)} e^{-i\omega_l(x_j-a)}, \quad \omega_l = \frac{2\pi l}{b-a}, \quad l = -\frac{M}{2}, \ldots, \frac{M}{2} - 1.$$

Finally, Step 3 requires the solution of (37) on a half-time step, from $t_n + \tau/2$ to $t_n + \tau$. Hence, the same expression as in step 1 is used, but with $\Psi^{(2)}$ as an initial condition. The result from this step corresponds to Ψ^{n+1}.

The method just presented is second-order accurate in time (due to the Strang splitting) and spectrally accurate in space. Its stability can be studied following the ideas in Bao et al. (2003). Let $\|\cdot\|_{l^2}$ be the discrete l^2-norm $\|\Psi\|_{l^2} = \sqrt{\frac{b-a}{M}\sum_{j=0}^{M-1}\left|\psi_j\right|^2}$. We get

$$\left\|\Psi^{n+1}\right\|_{l^2}^2 \leq e^{2\alpha\tau}\left\|\Psi^n\right\|_{l^2}^2,$$

which indicates that the method is unconditionally stable in the sense of Lax–Richtmyer.

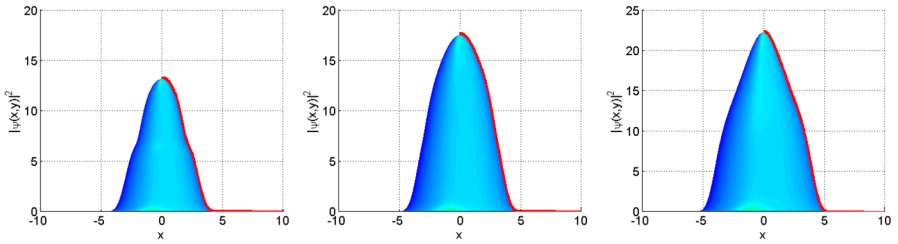

Fig. 10 Simulation results (density distributions, *blue*) and comparison with the collocation method (*red line*) for $R = 2$ (*left*), $R = 3$ (*center*), and $R = 4$ (*right*) (Color figure online)

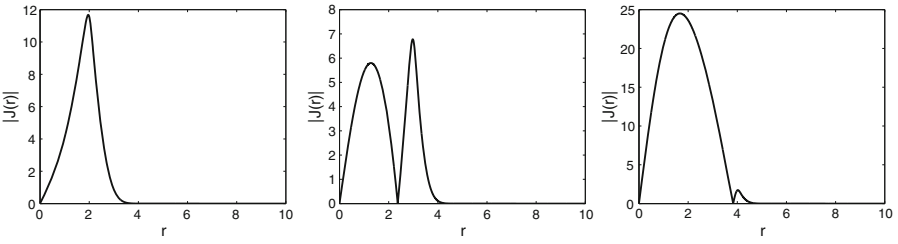

Fig. 11 Magnitude of the current J corresponding to the solutions for $R = 2$ (*left*), $R = 3$ (*center*), and $R = 4$ (*right*)

For all the methods presented so far, it is important to emphasize the use of the smooth Heaviside function. The original complex GP equation proposed by Keeling and Berloff (2008) includes a Heaviside function for the pumping part. With the latter, it is easy to see that the radially symmetric solutions have a discontinuity in the second derivative. This discontinuity reduces the accuracy of the collocation method and produces the Gibbs phenomenon in the splitting method due to the spectral part.

6.1 Simulation Results

The results corresponding to the 2D case are presented in this section. The integration domain is $[-15, 15] \times [-15, 15]$, with 1,024 divisions per axis and $\tau = 0.001$. The ground-state solution of the harmonic oscillator is used as an initial condition in these simulations.

For $R = 2, 3, 4$, the solutions are displayed in Fig. 10. In these cases, the system reaches the rotationally symmetric stationary-state as time evolves. This is the expected behavior, since it is shown in Sect. 4 that the radially symmetric solutions for $R = 2, 3, 4$ are stable. Also, Fig. 10 shows the comparison with the corresponding solutions obtained by the collocation method introduced in Sect. 3 (red line). Notice that both methods give the same result. Moreover, Fig. 11 shows the magnitude of the current, $|J|$, for these cases. Note that even for these radially symmetric solutions, the current exhibits complicated behavior.

For $R = 5$, the solution becomes unstable, as predicted in Sect. 3. Figure 12 shows the corresponding transient that, after breaking the symmetry, leads to the emergence

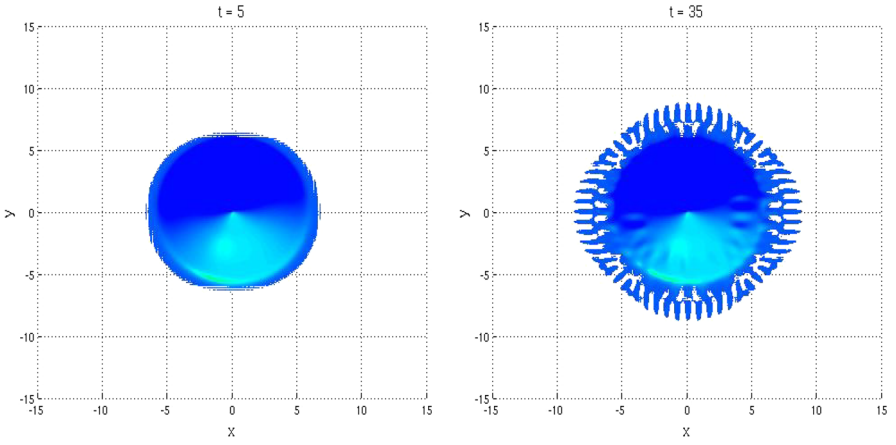

Fig. 12 Simulation results for $R = 5$ (see also the supplementary videos Sim1.avi and Sim2.avi). The *plots* show the density distribution at different times (continued in Fig. 13). The white areas represent regions where the density becomes zero. At the beginning, the condensate is confined in a radius approximately equal to 5. After breaking of symmetry, the condensate cloud experiences an expansion, and the remnants of this expansion can be seen at $R \gtrsim 5$. Notice that the white dots inside the region $R \lesssim 5$ at $t = 70$ correspond to the vortices that will eventually form the stable lattice. Some of these vortices are expelled out of the structure during the transient evolution

of vortex lattices. These vortex lattices remain rotating at a constant angular velocity, becoming the stable solution of the system (this simulation is also presented in the supplementary videos Sim1.avi and Sim2.avi.) Furthermore, Figs. 14, 15, 16, and 17 show the characteristics of these quantum vortices: The density profile drops to zero at the center of the vortex core, as shown in Fig. 14; the phase difference around the vortex is a multiple of 2π, as seen in Fig. 15 (left), where there is a change in the phase from 0 to 2π in all the vortices (indicated with blue circles); the condensate circulates around the vortex, as depicted in Fig. 16, where the current, J, is plotted for a central vortex (left) and a satellite vortex (right). Figure 17 shows the plot of $|\nabla\theta|$, the magnitude of the gradient of the phase, which is proportional to the velocity of the condensate. Notice that $|\nabla\theta| \approx 1/r$ around the core of the vortices. Finally, Fig. 18 shows the results for $R = 6, 7, 8$, and 9.

It is an interesting observation that the number of vortices that form in the simulations that start with a particular steady-state solution correlates with the most unstable azimuthal mode number, m, that is predicted by the linear stability analysis of Sect. 4. When the most unstable mode is m, the number of vortices that form tend to be close to m. For example, in Fig. 3b, the most unstable mode is around $m = 43$ and the corresponding vortex pattern shown in Fig. 18 consists of 43 vortices. For $R = 9$, a similar result was found with the maximum growth rate occurring at $m = 53$. Of course, in the absence of a full justification, this correspondence should be considered more as a coincidence. Particularly so because the vortices are intrinsically nonlinear, while the linear stability theory deals with infinitesimal perturbations to the steady state. In addition, we can see in Fig. 3b that there is a large number of modes which have growth rates very near that of the most unstable one. One should expect all modes

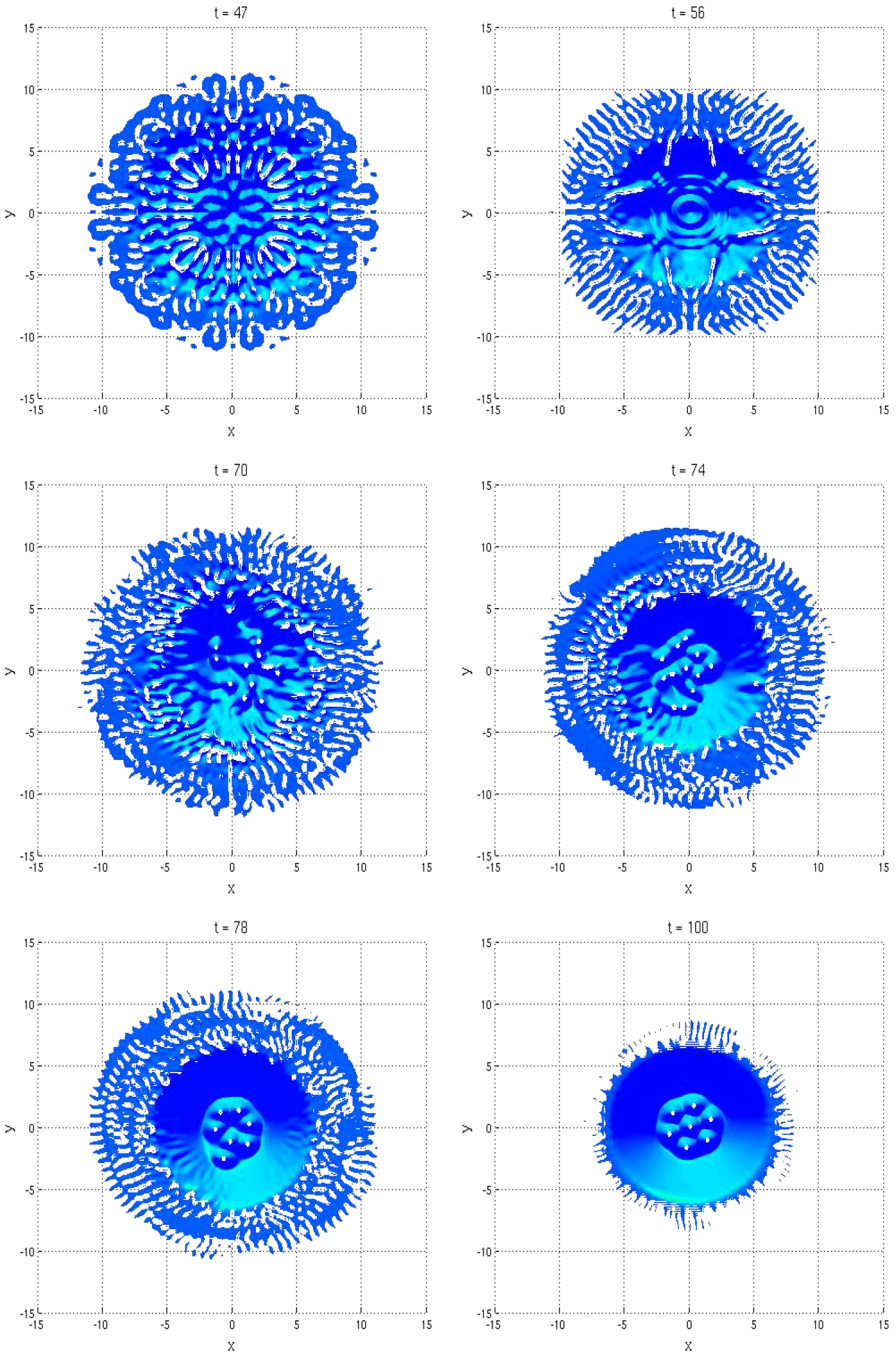

Fig. 13 Continuation of Fig. 12

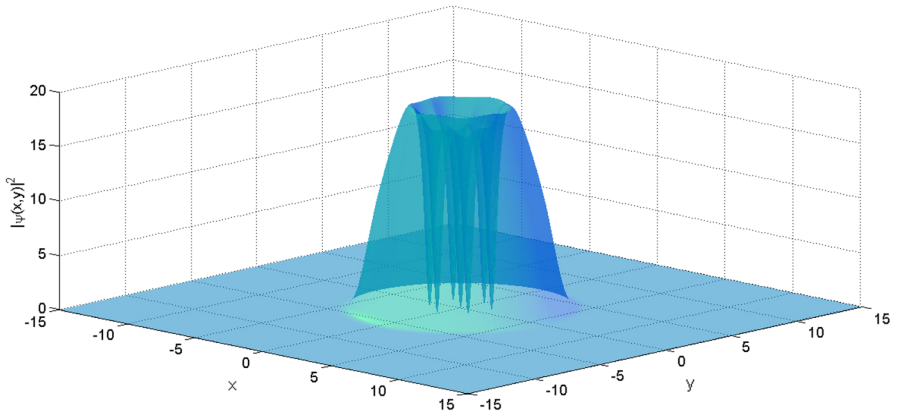

Fig. 14 Transparent image corresponding to the density distribution at $t = 140$ ($R = 5$)

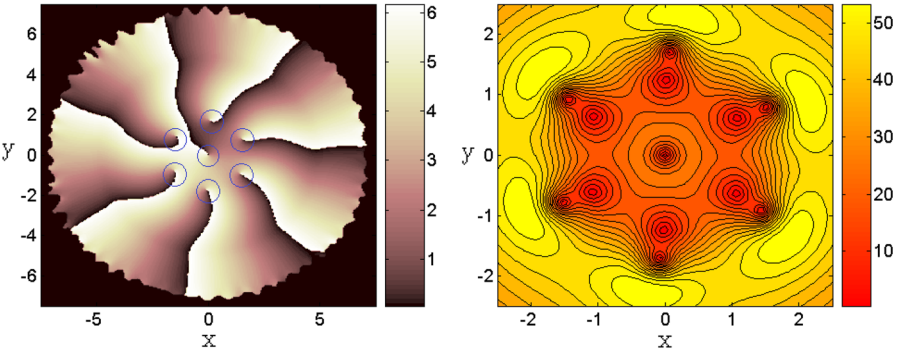

Fig. 15 *Left* Phase $\theta(x, y)$ of the solution at $t = 140$ ($R = 5$), with the *blue circles* indicating the core of the vortices. *Right* The magnitude of the current $|J(x, y)|$ at $t = 140$. Notice that the *contour lines* are closer around the core of the vortices (Color figure online)

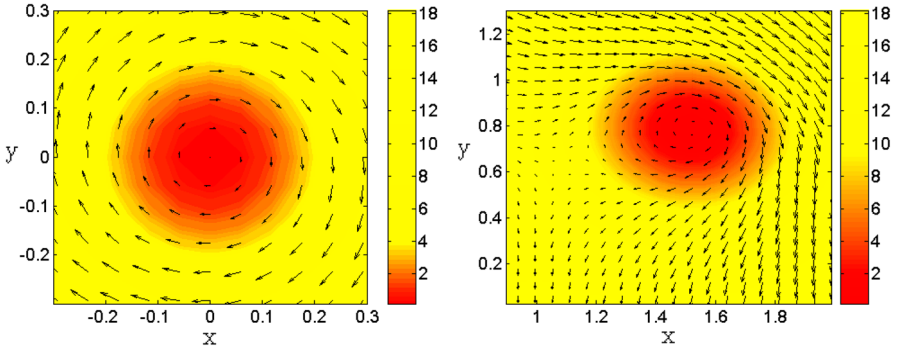

Fig. 16 Density distribution and arrows corresponding to the current J in the central vortex (*left*) and one satellite vortex (*right*) of the solution at $t = 140$ ($R = 5$)

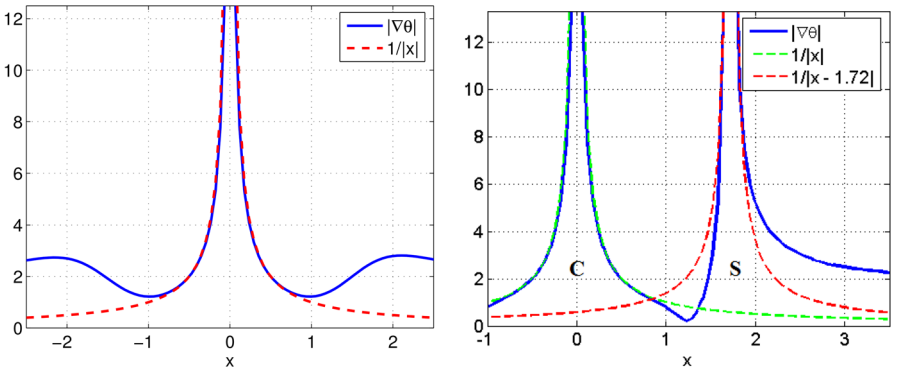

Fig. 17 1D plot for $|\nabla\theta|$ ($R = 5$): central vortex (*left*); central vortex "C" and satellite vortex "S" (*right*). For both central and satellite vortices, $|\nabla\theta| \approx 1/|x| = 1/r$ around the cores

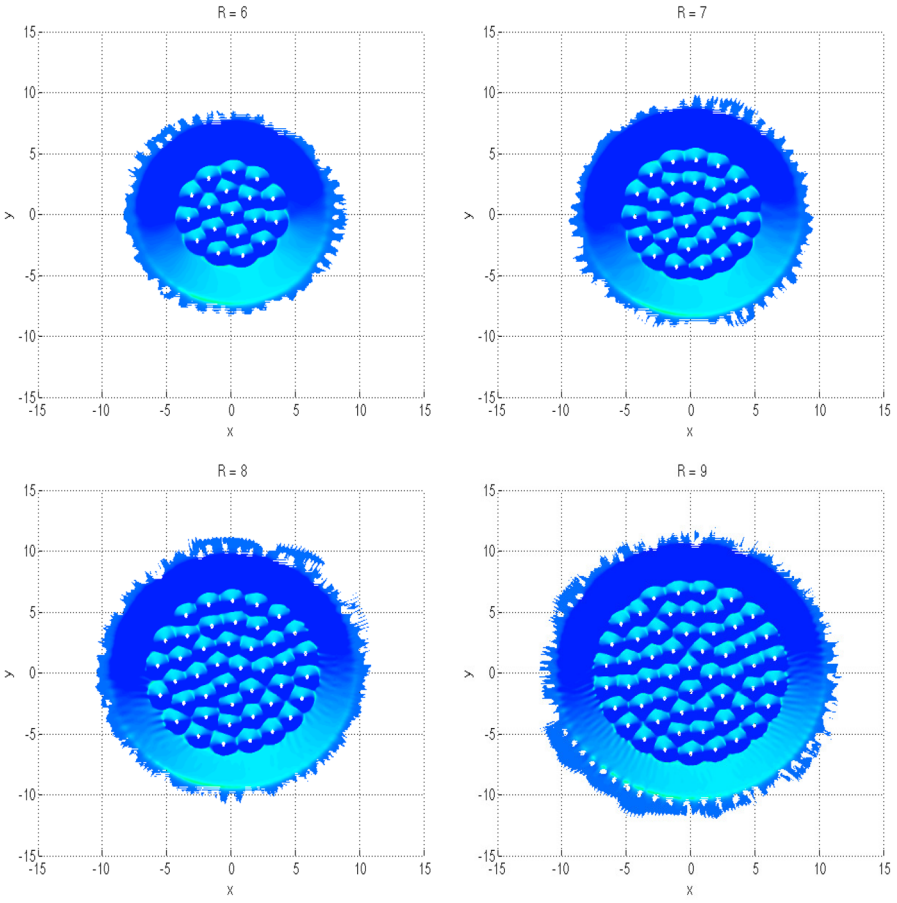

Fig. 18 Vortex lattices for $\alpha = 4.4$, $\sigma = 0.3$ and different values of R

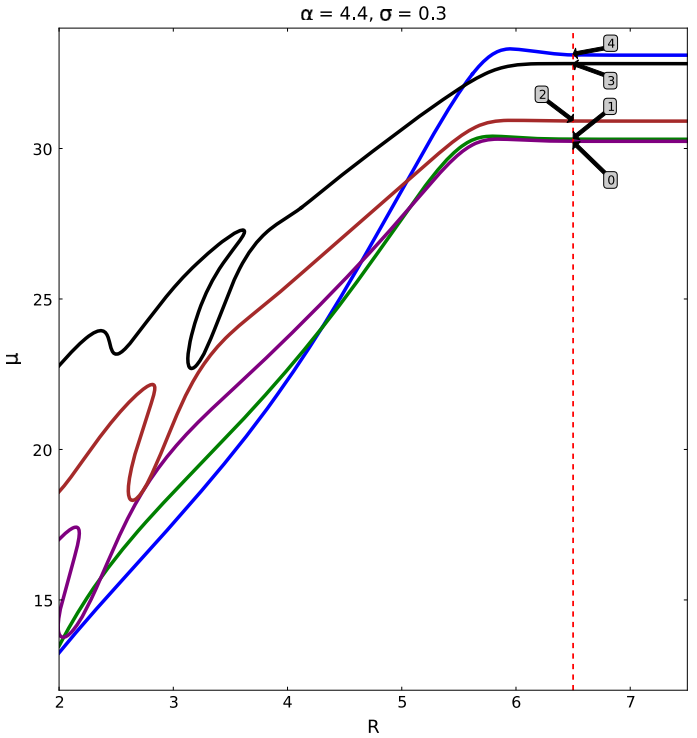

Fig. 19 Continuation in R starting from the solutions displayed in Figs. 8 and 9. The density profiles corresponding to the points labeled *0–4* are shown in Fig. 20

around $m = 40$–50 to play an important role in the nonlinear growth of instability toward the vortex patterns. Nevertheless, this correlation between the linear stability predictions and the final nonlinear patterns may be an indication of a closer connection between the two, perhaps pointing to the mechanism of the origin of the vortices.

It is also important to mention that experimental observations of vortex lattices are quite challenging unless some special configuration is chosen for the pumping function. With exactly the same configuration as used in our work, the vortices tend to rotate and it is experimentally difficult to resolve such motion (Borgh et al. 2012; Boulier et al. 2014). We point out a number of experiments where vortex patterns have been obtained. Boulier et al. (2014) observed a ring-shaped array of vortices when they injected angular momentum into the polariton fluid. Using multiple pumping spots arranged in a ring, Cristofolini et al. (2013) observed vortex patterns confined to the region within the ring. Manni et al. (2011) saw the formation of vortex arrays in a ring-shaped pumping region provided the pump power exceeded a certain threshold. In their theoretical calculations based on a version of the Gross–Pitaevskii equation, Manni et al. (2011) found that the number of vortices that form is sensitive to the size and the shape of the ring. Adding a central spot of the same intensity as the ring, Manni et al. (2013) obtained a spontaneous formation of vortex–antivortex pairs that arranged in a circular pattern.

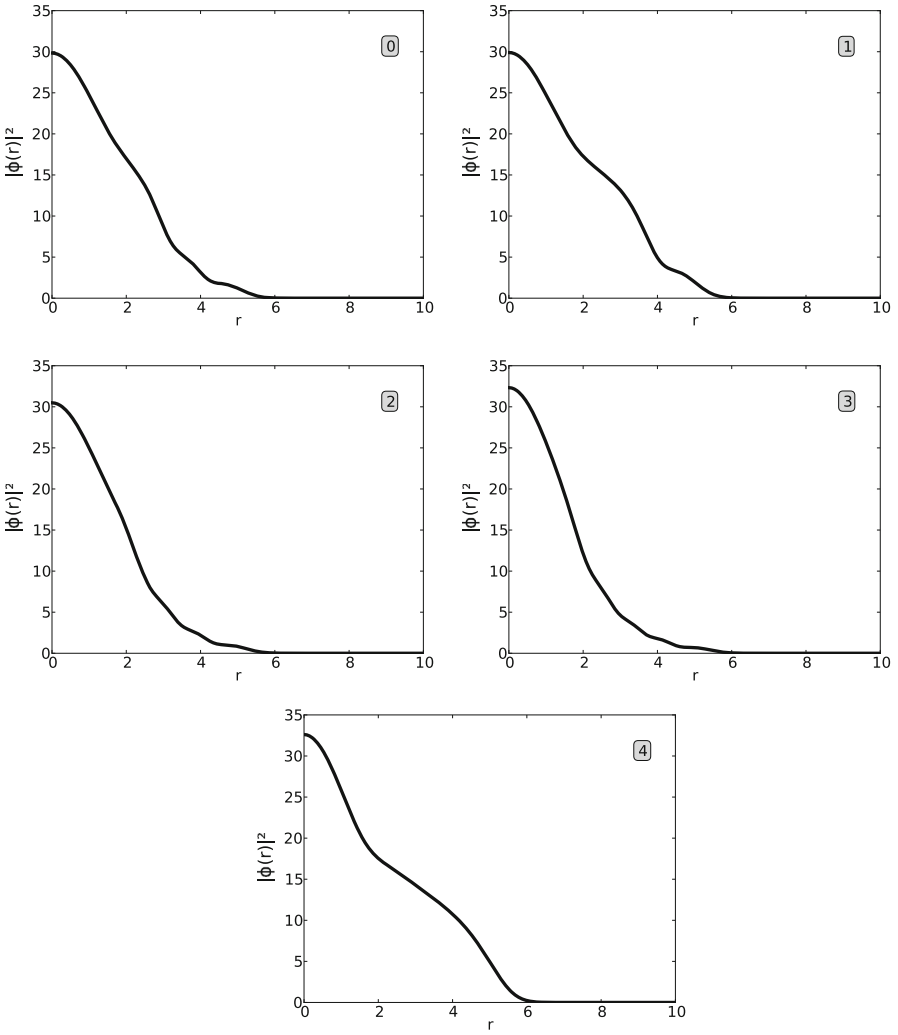

Fig. 20 Density profiles corresponding to the solutions labeled *0–4* in Fig. 19

6.2 Numerical Continuation in R

Figure 19 shows the continuation in R starting from the solutions displayed in Figs. 8 and 9. It can be seen that for all the branches, the solutions remain unchanged for large values of R. Moreover, the blue branch, which corresponds to the branch studied in the linear stability analysis performed in Sect. 4, has the smallest μ up to $R \simeq 4.4$. This is also the point at which the branch becomes linearly unstable, as shown in Fig. 5. On the other hand, Fig. 20 shows the density profiles corresponding to the solutions labeled 0 to 4 in Fig. 19. Notice that although the continuation process started in the multi-bump profiles shown in Figs. 8 and 9, these solutions do not have this multi-bump

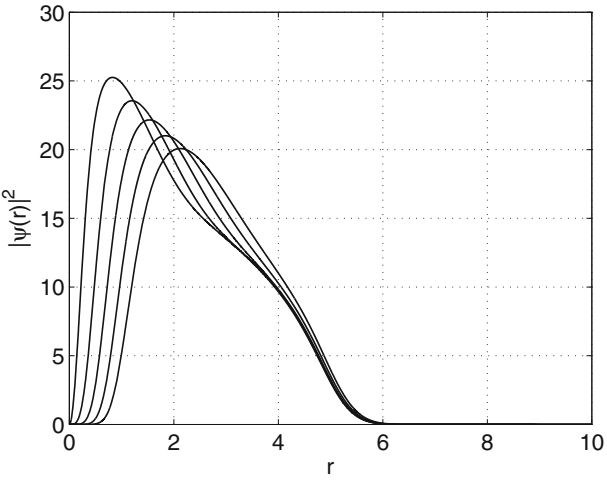

Fig. 21 Density distributions corresponding to the central vortex states for $\alpha = 4.4$, $\sigma = 0.3$, $R = 5$, and $m = 1$ to 5 (in order of decreasing peaks)

characteristic. Also, the blue branch is not the one with the smallest μ for large values of R. In any case, for large values of R, none of these radially symmetric solutions is linearly stable. It is interesting to observe that even though the radially symmetric solutions remain unchanged for large values of R, the stable vortex lattice solutions change as R increases, as seen in Fig. 18.

6.3 Central Vortex States

Let us now investigate the existence of central vortex states similar to the ones observed in a rotating BEC (Bao et al. 2005). To find these states, consider solutions of (1) of the form $\psi(x,t) = e^{-i\mu t}\psi_m(x) = e^{-i\mu t}\psi_m(r)\,e^{im\theta}$, where μ is the chemical potential and $m = 1, 2, 3, \ldots$ is called the winding index. Introducing this ansatz into (1) gives the following equation for ψ_m:

$$\mu\psi_m(r) = \left[-\frac{1}{r}\frac{\mathrm{d}}{\mathrm{d}r}\left(r\frac{\mathrm{d}}{\mathrm{d}r}\right) + \frac{m^2}{r^2} + V(r) + |\psi_m(r)|^2 + i\left(\alpha\Theta_R - \sigma\,|\psi_m(r)|^2\right)\right]\psi_m(r), \tag{44}$$

with

$$\psi_m(0) = 0, \quad \lim_{r\to\infty}\psi_m(r) = 0.$$

This problem is solved by the collocation method described in Sect. 3. Figure 21 shows the results for $\alpha = 4.4$, $\sigma = 0.3$, $R = 5$, and $m = 1$ to 8. To study their linear stability, small perturbations of the wave function can be expressed as

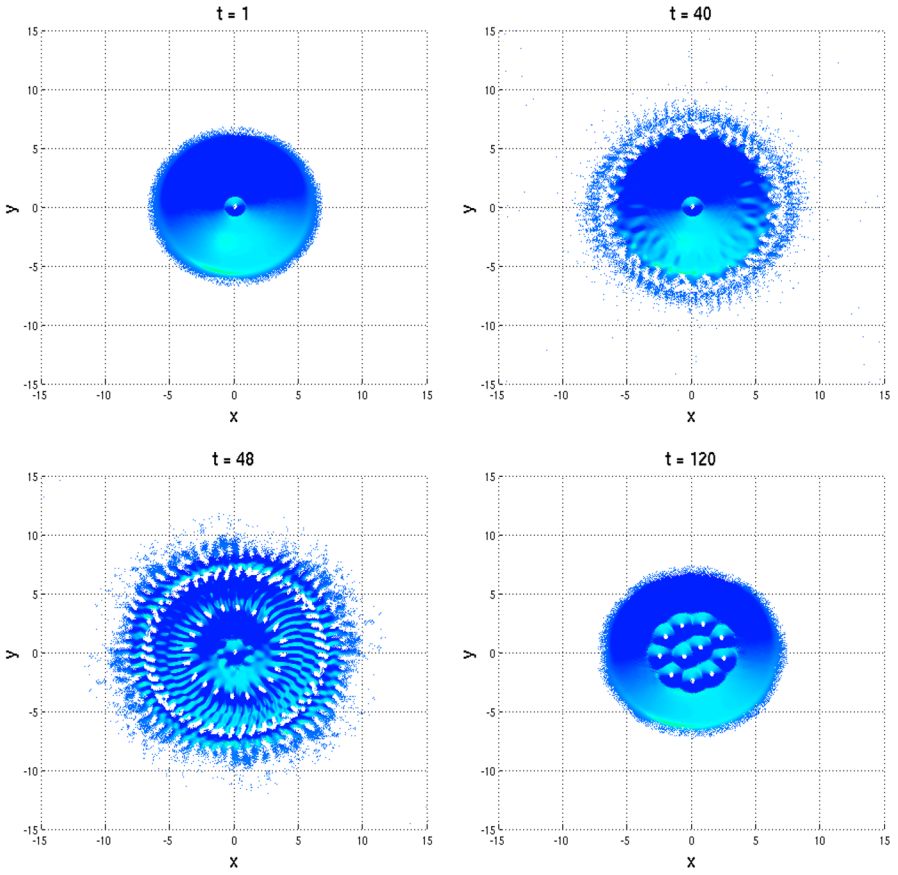

Fig. 22 Simulation result for the $m = 1$ central vortex state (see also supplementary video Sim3.avi)

$$\psi(r,\theta,t) = e^{-i\mu t}\left[\psi_m(r)\, e^{im\theta} + \varepsilon\left(u(r)e^{i(n\theta-\omega t)} + v^*(r)\, e^{i(n\theta+\omega^* t)}\right)\right], \quad \times \quad n = 1, 2, \ldots, \tag{45}$$

with $\varepsilon \to 0$. The perturbation is time dependent with frequency ω and the complex amplitude functions $u(r)$ and $v(r)$. Proceeding as in the linear stability analysis performed in Sect. 4 with $n = 1, \ldots, 50$, it can be shown that all of the central vortex states displayed in Fig. 21 are linearly unstable. When these central vortex states are used as initial conditions for the Strang-splitting spectral method, it is possible to study the manifestation of these instabilities. In particular, Figs. 22 and 23 show the results for $m = 1, 2$. The $m = 1$ vortex appears stable for a long time, and then, it undergoes symmetry breaking and gives rise to a vortex lattice. The $m = 2$ vortex has an additional interesting behavior: It appears stable for a short time; the vortex then splits into two $m = 1$ vortices; and finally, this solution breaks and generates a vortex lattice. Such splitting for $m = 2$ was observed experimentally in Sanvitto et al. (2010) in an exciton–polariton condensate.

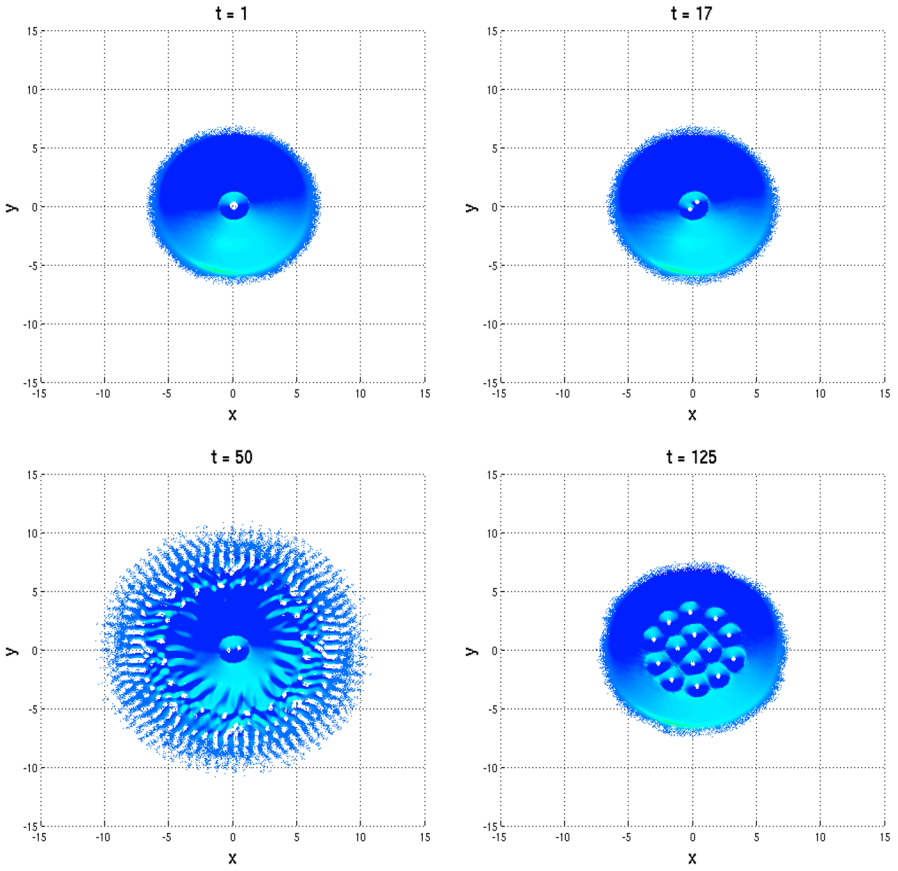

Fig. 23 Simulation result for the $m = 2$ central vortex state (see also supplementary video Sim4.avi)

7 Conclusions

The general behavior of the 2D complex GP equation was presented using different numerical techniques. The first step for the numerical characterization of this equation was the analysis of its radially symmetric solutions. Due to the lack of conservation of mass and energy, the standard techniques used for the study of the radially symmetric ground-state solution of the GP equation, such as the gradient flow method, do not apply in this case. In order to overcome this problem, the stationary complex GP Eq. (3) was studied directly using a collocation method. Once the radially symmetric solutions were obtained, their linear stability was investigated. Afterward, numerical continuation was applied to one of the linearly stable solutions to study its excited states. We found that the linearly stable solution has the smallest chemical potential in the group of solutions found, which leads us to define it as the ground state of the system and the rest of the solutions as excited states. However, a rigorous definition of the energy is required to corroborate this statement.

We used numerical integration to study the nonlinear evolution of the linearly unstable solutions. We observed the emergence of complicated vortex lattices after symmetry breaking (as in Keeling and Berloff 2008). These lattices remain rotating with a constant angular velocity, becoming the stable solution of the system.

The phenomenon of vortex-pattern formation seems to be well described by the complex GP equation. However, from a rigorous mathematical point of view, proving stability results for this equation is complicated. The complex GP equation can be thought of as a complex Ginzburg–Landau equation without viscous dissipation. The absence of this dissipation makes it difficult even to get time-uniform estimates of the solutions of this equation in an appropriate energy space. As a consequence, until now, the study of the attractor and its stability cannot be carried out (see Temam 1997 for a general background on these topics).

Finally, we computed the central vortex solutions of the complex GP equation. An interesting result was the splitting of the $m = 2$ central vortex into two $m = 1$ vortices, which was observed experimentally by Sanvitto et al. (2010) in a Bose–Einstein condensation of exciton–polaritons. We thus see the rich behavior of the complex GP equation, which somehow combines the characteristics of both the GP and the complex Ginzburg–Landau equations.

Acknowledgments J. S., A. K., and P. M. gratefully acknowledge research support by King Abdullah University of Science and Technology (KAUST). The first author acknowledges the assistance and comments from W. Bao, D. Ketcheson, P. Antonelli, N. Berloff, F. Pinsker, B. Sandstede, B. Oldeman, and the Research Computing Group from KAUST. The work of the last author has been supported by the Hertha-Firnberg Program of the FWF, Grant T402-N13.

References

Amo, A., Lefrère, J., Pigeon, S., Adrados, C., Ciuti, C., Carusotto, I., Houdré, R., Giacobino, E., Bramati, A.: Superfluidity of polaritons in semiconductor microcavities. Nat. Phys. **5**(11), 805–810 (2009)

Anderson, M., Ensher, J., Matthews, M., Wieman, C., Cornell, E.: Observation of Bose-Einstein condensation in a dilute atomic vapor. Science **269**(5221), 198–201 (1995)

Antonelli, P., Carles, R., Sparber, C.: On nonlinear Schrödinger type equations with nonlinear damping. arXiv preprint arXiv:1303.3033 (2013)

Ascher, U.M., Mattheij, R.M., Russell, R.D.: Numerical Solution of Boundary Value Problems for Ordinary Differential Equations, volume 13. Society for Industrial and Applied Mathematics, Philadelphia (1987)

Ballarini, D., Sanvitto, D., Amo, A., Viña, L., Wouters, M., Carusotto, I., Lemaitre, A., Bloch, J.: Observation of long-lived polariton states in semiconductor microcavities across the parametric threshold. Phys. Rev. Lett. **102**(5), 056402 (2009)

Bao, W., Jin, S., Markowich, P.A.: On time-splitting spectral approximations for the Schrödinger equation in the semiclassical regime. J. Comput. Phys. **175**(2), 487–524 (2002). ISSN 0021–9991

Bao, W., Jaksch, D., Markowich, P.A.: Numerical solution of the Gross-Pitaevskii equation for Bose–Einstein condensation. J. Comput. Phys. **187**(1), 318–342 (2003). ISSN 0021–9991

Bao, W., Jaksch, D., Markowich, P.A.: Three-dimensional simulation of jet formation in collapsing condensates. J. Phys. B At. Mol. Opt. Phys. **37**(2), 329 (2004)

Bao, W., Wang, H., Markowich, P.A.: Ground, symmetric and central vortex states in rotating Bose–Einstein condensates. Commun. Math. Sci. **3**(1), 57–88 (2005)

Borgh, M., Franchetti, G., Keeling, J., Berloff, N.: Robustness and observability of rotating vortex lattices in an exciton-polariton condensate. Phys. Revi. B **86**(3), 035307 (2012)

Bose, S.: Plancks gesetz und lichtquantenhypothese. Z. phys **26**(3), 178 (1924)

Boulier, T., Terças, H., Solnyshkov, D., Glorieux, Q., Giacobino, E., Malpuech, G., Bramati, A.: Annular vortex chain in a resonantly pumped polariton superfluid. arXiv preprint arXiv:1405.1375 (2014)

Bradley, C., Sackett, C., Tollett, J., Hulet, R.: Evidence of Bose–Einstein condensation in an atomic gas with attractive interactions. Phys. Rev. Lett. **75**(9), 1687 (1995)
Bramati, A., Modugno, M.: Physics of Quantum Fluids. New Trends and Hot Topics in Atomic and Polariton Condensates. Springer, Berlin (2013)
Brunner, H.: Collocation Methods for Volterra Integral and Related Functional Differential Equations, volume 15. Cambridge University Press, Cambridge (2004)
Coldren, L., Corzine, S.: Diode Lasers and Photonic Integrated Circuits, volume 218. Wiley Series in Microwave and Optical Engineering, New York (1995)
Cristofolini, P., Dreismann, A., Christmann, G., Franchetti, G., Berloff, N., Tsotsis, P., Hatzopoulos, Z., Savvidis, P., Baumberg, J.: Optical superfluid phase transitions and trapping of polariton condensates. Phys. Rev. Lett. **110**(18), 186403 (2013)
Cuevas, J., Rodrigues, A.S., Carretero-González, R., Kevrekidis, P.G., Frantzeskakis, D.J.: Nonlinear excitations, stability inversions, and dissipative dynamics in quasi-one-dimensional polariton condensates. Phys. Rev. B **83**(24), 245140 (2011)
Davis, K., Mewes, M., Andrews, M., van Druten, N., Durfee, D., Kurn, D., Ketterle, W.: Bose–Einstein condensation in a gas of sodium atoms. Phys. Rev. Lett. **75**(22), 3969–3973 (1995)
De Hoog, F.R., Weiss, R.: Difference methods for boundary value problems with a singularity of the first kind. SIAM J. Numer. Anal. **13**(5), 775–813 (1976)
Doedel, E.J., Paffenroth, R.C., Champneys, A.R., Fairgrieve, T.F., Kuznetsov, Y.A., Oldeman, B.E., Sandstede, B., Wang, X.J.: Auto-07p: continuation and bifurcation software for ordinary differential equations (2007). http://indy.cs.concordia.ca/auto
Einstein, A.: Sitzungsberichte der preussischen akademie der wissenschaften. Physikalisch-mathematische Klasse **261**(3) (1924)
Einstein, A.: Quantum theory of the monoatomic ideal gas. Sitzungsber. Preuss. Akad. Wiss, page 261 (1925)
Gasser, I., Markowich, P.: Quantum hydrodynamics, Wigner transforms, the classical limit. Asymptot. Anal. **14**(2), 97–116 (1997)
Govaerts, W.J.F.: Numerical methods for bifurcations of dynamical equilibria. Number 66. SIAM, Philadelphia (2000)
Gross, E.: Hydrodynamics of a superfluid condensate. J. Math. Phys. **4**, 195 (1963)
Kasprzak, J., Richard, M., Kundermann, S., Baas, A., Jeambrun, P., Keeling, J., Marchetti, F., Szymanacute, M., Andre, R., Staehli, : Bose–Einstein condensation of exciton polaritons. Nature **443**(7110), 409–414 (2006)
Keeling, J., Berloff, N.: Exciton-polariton condensation. Contemp. Phys. **52**(2), 131–151 (2011)
Keeling, J., Berloff, N.G.: Spontaneous rotating vortex lattices in a pumped decaying condensate. Phys. Rev. Lett. **100**(25), 250401 (2008). ISSN 1079–7114
Keller, H.B.: Numerical solution of bifurcation and nonlinear eigenvalue problems. In: Rabinowitz, P.H. (ed.) Applications in Bifurcation Theory, pp. 359–384. Academic Press, New York, San Francisco, London (1977)
Keller, H.B.: Lectures on numerical methods in bifurcation problems. Appl. Math. **217**, 50 (1987)
Manni, F., Lagoudakis, K., Liew, T., André, R., Deveaud-Plédran, B.: Spontaneous pattern formation in a polariton condensate. Phys. Rev. Lett. **107**(10), 106401 (2011)
Manni, F., Liew, T., Lagoudakis, K., Ouellet-Plamondon, C., André, R., Savona, V., Deveaud, B.: Spontaneous self-ordered states of vortex-antivortex pairs in a polariton condensate. Phys. Rev. B **88**(20), 201303 (2013)
Ohadi, H., Kammann, E., Liew, T., Lagoudakis, K., Kavokin, A., Lagoudakis, P.: Spontaneous symmetry breaking in a polariton and photon laser. Phys. Rev. Lett. **109**(1), 016404 (2012)
Pitaevskii, L.: Vortex lines in an imperfect Bose gas. Sov. Phys. JETP **13**(2), 451–454 (1961)
Pitaevskii, L., Stringari, S.: Bose-Einstein Condensation. Number 116. Oxford University Press, Oxford (2003)
Sanvitto, D., Marchetti, F.M., Szymanska, M.H., Tosi, G., Baudisch, M., Laussy, F.P., Krizhanovskii, D.N., Skolnick, M.S., Marrucci, L., Lemaitre, A., Bloch, J., Tejedor, C., Vina, L.: Persistent currents and quantized vortices in a polariton superfluid. Nat. Phys. (2010). ISSN 1745-2473
Temam, R.: Infinite Dimensonal Dynamical Systems in Mechanics and Physics, vol. 68. Springer, Berlin (1997)
Wouters, M., Carusotto, I.: Excitations in a nonequilibrium Bose-Einstein condensate of exciton polaritons. Phys. Rev. Lett. **99**(14), 140402 (2007)